

## Supplementary Information

to

### **Crumpled Sheets of Reduced Graphene Oxide as a Highly Sensitive, Robust and Versatile Strain/Pressure Sensor**

Subhajit Kundu,<sup>a</sup> S. Rammohan,<sup>b</sup> Kazi Rafsanjani Amin,<sup>c</sup> Aweek Bid,<sup>c</sup> Rudra Pratap<sup>b</sup> and N. Ravishankar<sup>a\*</sup>

**Affiliations:**

<sup>a</sup>Materials Research Centre, Indian Institute of Science, Bangalore, India, 560012.

<sup>b</sup>Centre for Nano Science and Engineering, Indian Institute of Science, Bangalore, India, 560012.

<sup>c</sup>Department of Physics, Indian Institute of Science, Bangalore, India, 560012.

\*Correspondence to: [nravi@mrc.iisc.ernet.in](mailto:nravi@mrc.iisc.ernet.in)

## I. Comparison of Gauge Factor with literature:

*Table S1: Comparison of Gauge Factor of the strain sensor with other sensors reported in literature showing ultra-high Gauge Factor at strains of the order  $10^{-4}$ .*

<b>Journal , Year</b>	<b>Principle</b>	<b>G.F.</b>	<b>Strain</b>
Nat. Mat. 2012 <sup>1</sup>	Reversible interlocking of fibres	11.45 (w.r.t. vertical strain)	0-2%
Nat. Nano. 2011 <sup>2</sup>	Aligned CNT array	15	1%
ACS Nano 2015 <sup>3</sup>	Nanohybrid of CNT and conducting elastomer	39.4	>1.5%
ACS Nano 2014 <sup>4</sup>	Silver Nanowire_Elastomer Nanocomposite	2-14	70% stretchable
Nano Lett. 2015 <sup>5</sup>	Metal nanowire percolation network	>20	~35%
Nano Lett. 2012 <sup>6</sup>	Overlapping 2D graphene sheets	>150	0-2%
ACS Nano 2015 <sup>7</sup>	CNT in polymer	0.56	0-200%
Sci. Rep. 2012 <sup>8</sup>	Graphene on polymer	~10 <sup>3</sup>	2~6%
Nano Lett. 2012 <sup>9</sup>	Percolating nanotube network (Capacitive)	0.99	Till 100%
Nat. Comm. 2014 <sup>10</sup>	Au nanowire impregnated tissue paper	7.38 (w.r.t. vertical strain)	Till 14%
Nano Lett. 2008 <sup>11</sup>	Single ZnO piezoelectric nanowire	<400	0.2%
Nat. Nano 2011 <sup>12</sup>	Transparent elastic films of CNT(Capacitive)	1250 0.004	1% 0-50%
<b>Present Study</b>	<b>Crumpled rGO sheets</b>	<b>&gt;4000</b>	<b>0.02%</b>

## **II. SEM and TEM images of rGO:**

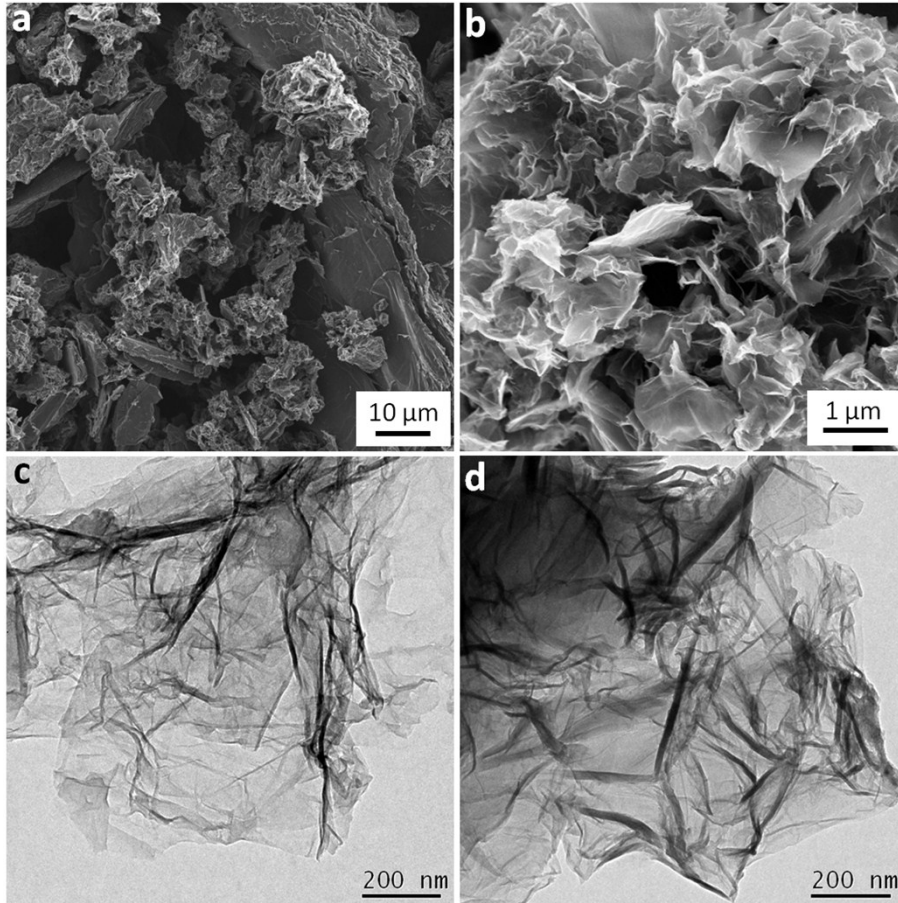


***Figure S1: (a), (b) SEM & (c), (d) TEM images of crumpled rGO.***

### III. Sensing of strain and pressure with taped crumpled rGO:

#### III.I. Sensing of strain:

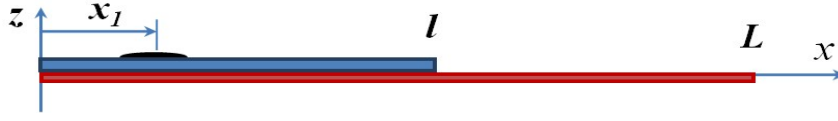


**Figure S2:** Schematic of rGO based strain sensor bonded to a cantilever beam of length  $L$  for measuring the strain at the location of interest  $x_1$ .

The structure used in the experiments is a cantilever beam with the sensor located close to the fixed end as shown in the schematic in Fig. S2. The length of the Kapton strip and the bottom substructure are taken as  $l$  and  $L$  respectively. The free end of the cantilever is given a known transverse displacement ( $\delta$ ) to strain the beam. The strain in  $x$  direction as a function of the given location  $x_1$  and height  $z$  for a given transverse displacement  $\delta$  in  $z$  direction at the end  $x = L$  is obtained in terms of the device dimensions and material properties as follows:

$$\varepsilon_{11} = -z \frac{3EI_2(x_1 - L)}{EI_1(l - L)^3 - EI_2(l^2 - 3lL + 3L^2)} \delta \quad \text{eqn. (1)}$$

where  $EI_1$  denotes the equivalent flexural rigidity of the segment of the beam up to  $x = l$  and  $EI_2$  indicates the flexural rigidity of the segment of the beam from  $x = l$  to  $x = L$ . If  $E_i$ ,  $A_i$  and  $t_i$  represent Young's modulus, cross sectional area and thickness of  $i^{\text{th}}$  layer, then the equivalent flexural rigidity of the first segment is given as:

$$EI_1 = E_1 A_1 \frac{t_1^2}{12} + E_2 A_2 \frac{t_2^2}{12} + \frac{E_1 A_1 E_2 A_2}{E_1 A_1 + E_2 A_2} \left( \frac{t_1 + t_2}{2} \right)^2 \quad \text{eqn. (2)}$$

#### III.II. Effect of strain on the sensor:

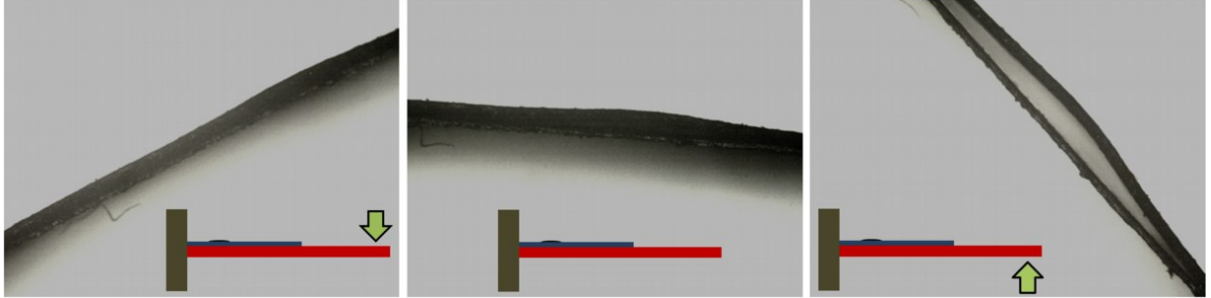


**Figure S3:** Cross-sectional optical microscopy of the sensor (rGO/tape region) while under positive, zero and negative strain.

**Change in cross-sectional area of the rGO patch on bending:** Cross-sectional optical microscope images have been acquired at positive and negative strained condition of the sensor (Fig. S3). The relative change in the area is much higher for the case of negative strain than that of positive strain.

**Effect of area change on the contacts between the rGO particles:** The considerable change in the resistance on compressive straining of the sensor is the result of separation of the conducting particles of rGO. The qualitative description of percolation network is obtained from the cross-

sectional SEM images of the sensor. The sensor is deflected by known amount and SEM images of rGO are taken at same location. The images are processed in MATLAB to determine the edges of rGO particles and their distribution with end displacement. The edge length and the number of edges for three end displacements are shown in Fig. S4. It can be noted from the Fig. that the increase in number of edges indicates the possible separation happening between rGO particles. Hence, it can be qualitatively asserted from the SEM images that the increase in resistance during concave bending is due to the separation of particles resulting in contact loss.

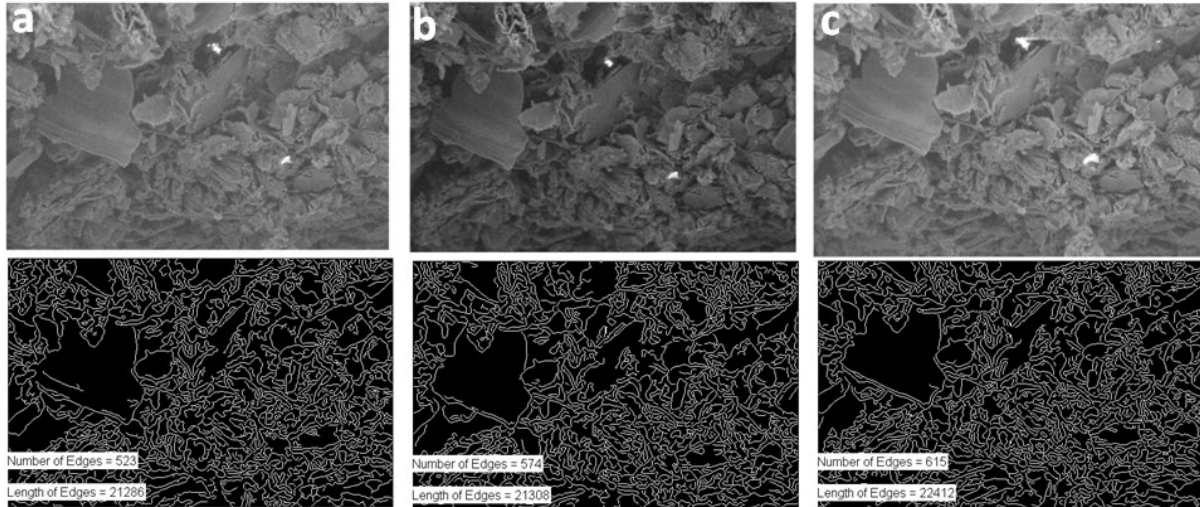


**Figure S4:** Cross-sectional SEM images of the rGO patch as the cantilever bends. The cantilever is given an end displacement (concave bending) of 1 mm, 2 mm, and 3 mm such that the packing of the rGO particles relax. The SEM image and the corresponding processed image with number of edges and the length of edges ( $10^{-8}$  m) is shown respectively in (a), (b), and (c). Increase in the number of edges indicates the separation between the adjacent rGO particles.

### III.III. Simulation details :

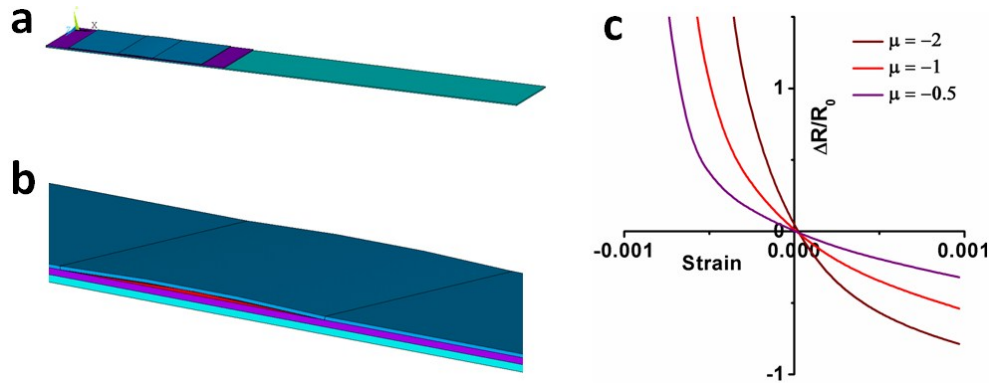


**Figure S5:** (a), (b) ANSYS Model of a rGO strain sensor. The sensing element (rGO) is sandwiched between top adhesive layer and Kapton sheet. The Kapton is further bonded to a copper substrate. (c) The relative change in resistance as a function of strain at different values of the transport exponent as predicted by the model. It shows a similar trend as obtained experimentally.

rGO sensor manifests the change in strain by the corresponding change in resistance. The sensor is capable of measuring both compressive and tensile strains. However, it is more sensitive to compressive strains than tensile strains. This results in extremely large values of gauge factor in compression than in tension. This non-uniform change in the resistance in compressive and tensile strains is described using a percolation model. The percolation model of the sensor requires the determination of critical volume of the sensor element beyond which the conductivity is lost. Denoting the critical partial volume  $v_c$  of rGO as the percolation threshold, the critical volumetric strain  $\gamma_c$  of rGO sensor as a function of initial partial volume  $v_0$  is given as

$$\gamma_c = 1 - \frac{v_0}{v_c}. \quad \text{eqn. (3)}$$

A percolation model for conductivity of a composite with conductive inclusions in an insulator matrix is discussed by Chelidze et. al.<sup>13</sup> However, the critical volume in the present case is the largest volume of the sensing element where resistance of sensor is highest. Following the procedure described, the instantaneous partial volume  $v$  of the sensing element is related to the corresponding volumetric strain  $\gamma$  as

$$\frac{v - v_c}{v_c} = \frac{\gamma - \gamma_c}{1 - \gamma}. \quad \text{eqn. (4)}$$

The model for electrical conductivity  $\sigma$  as per the universal scaling law described by Sahimi<sup>14</sup> is written in terms of the change in the volume as

$$\sigma(v) \approx |v - v_c|^\mu. \quad \text{eqn. (5)}$$

where  $\mu$  is transport exponent. From eqn. (4) and eqn. (5), the change in resistance as a function of volumetric strain of the sensor is

$$R(\gamma) = r_c \left| \frac{\gamma - \gamma_c}{1 - \gamma} \right|^{-\mu}. \quad \text{eqn. (6)}$$

where  $r_c$  is a proportionality constant evaluated from the initial unstrained condition. The relative change in resistance for three values of  $\mu$  is shown in Fig. S5c. The transport exponent  $\mu$ ,<sup>13</sup> in the

present case, close to 0.5 fits well with the experimental data. The volumetric strains of sensing element are determined using a finite element model of the rGO sensor.

The rGO sensing element placed on a Kapton film is bonded to a copper strip of length 50 mm. The complete solid model is shown in Fig. S5a. The detailed description of layers is shown in Fig. S5b. The beam is clamped at the end closer to the sensor. The free end of the beam is given a displacement of 2 mm, and 4 mm in transverse direction and the corresponding longitudinal strains at the sensing element are determined. Similarly, the longitudinal strains for negative transverse displacements are determined. The volume of rGO sensing element is tabulated for every deformation in Table S2. The value of  $\gamma_c$  is calculated from eqn. (3) and the value of  $r_c$  is calculated from eqn. (6) by using the value of base resistance in undeformed configuration. The resistance is then estimated (Fig. S5c) using the eqn. (6) and compared with the experimental values.

**Table S2:** Volume of the rGO sensing element for each deflection of the cantilever.

End Displacement (mm)	rGO Volume (mm <sup>3</sup> )	Volumetric Strain ( $\gamma$ )	Longitudinal Strain ( $\epsilon_x$ %)
-4	0.963	0.204	-0.112
-2	0.867	0.083	-0.049
0	0.800	0.000	0.000
2	0.739	-0.076	0.045
4	0.668	-0.165	0.097

#### **III.IV Application of the strain sensor- Predicting the breaking of glass:**

In a typical experiment, a standard glass slide of thickness 1 mm (length- 7.5 cm & breadth- 2.5 cm) is placed in between two supports separated by a distance of 5 cm as shown in the inset of Fig. 1d. The sensor is pasted on the glass slide at a point half way along the length and at a side along the breadth. Force is applied (UTM) using a flat punch of area 2 mm X 1 mm at the centre of the glass slide (not on the sensor) to strain it. The strain in glass is calculated using the displacement data which is shown in the Table S3. The corresponding current at a fixed voltage is acquired using a Keithley source meter interfaced with a computer.

**Table S3:** Strain at the centre of the glass slide at each value of force.

F (N)	Strain
0	0
10.1	-0.00046
20.1	-0.00091
30.1	-0.00137
40	-0.00182

### III.V. Response of a similar sensor to pressure:

Gentle tapping of the sensor with finger shows an increase in current (Fig. S6) indicating that it can be used for sensing pressure. For better quantification of the response, the sensor was kept under the universal testing machine (UTM) connected to a load cell (Max. force- 500 N and resolution  $\sim 83$  mN) for applying pressure (Fig. S6b). The force and displacement vs time is simultaneously recorded (Approach rate -1 mm/s). A Keithley source meter was used to bias (1 V) the sensor with a fixed voltage and measure the current at the corresponding times using Labview program.

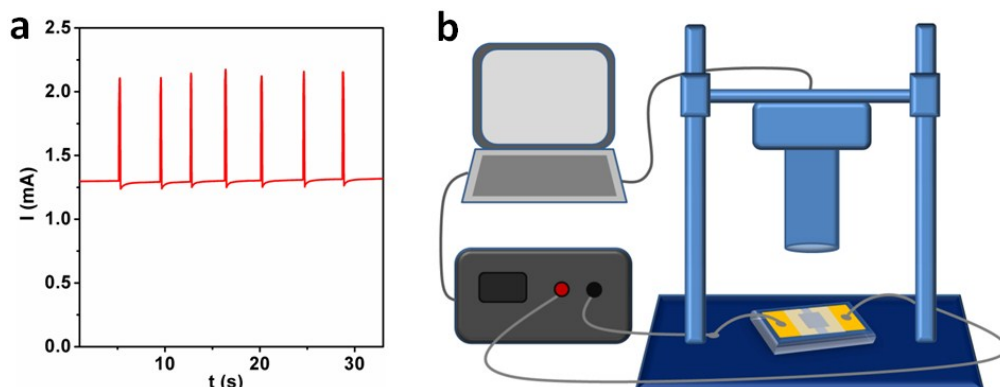


**Figure S6:** (a) Current response of the sensor to gentle tapping with finger indicating that the taped crumpled rGO aggregate can be used in detection of pressure. (b) Schematic showing the experimental setup to quantify the response of the sensor to pressure.

### III.VI. Effect of pressure on rGO aggregate:

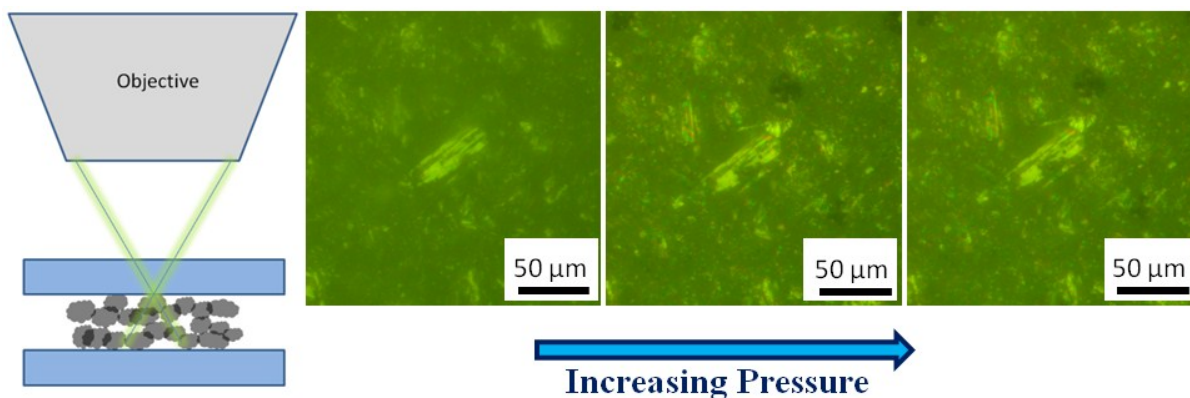


**Figure S7:** Optical microscopy of unpressed and pressed crumpled rGO between glass slides. Compression shows up more rGO in the plane of focus indicating better contact among the rGO grains.

## IV. Dynamic response of the sensor:

### IV.I. Detection of dynamic strain:

#### **Tests on vibrating cantilever:**

To test the dynamic response of the sensor, it was integrated over a steel/copper cantilever beam that was mounted over a speaker (Fig. S8a). A sinusoidal input voltage,  $V_{pp}$  (peak to peak voltage) of 1 V was applied to the speaker at different frequencies (around the resonance frequency of the cantilever) starting from 26 Hz to 30 Hz was applied to set the cantilever into vibration. The vibration of the cantilever was monitored using laser doppler vibrometry (LDV). The temporal strain ( $\delta$ ) at the sensing element was computed from the measured velocity. For the response, the sensor was biased with a fixed voltage of 0.1 V and the corresponding current was recorded using probe station.

The amplitude of vibration and hence the maximum strain in each cycle varies with frequency. Fig. S8b shows the variation of relative change in resistance of the sensor with strain. The corresponding variation of gauge factor with strain is shown in Fig. S8c. The variation of the relative change in resistance and the gauge factor with strain shows a similar trend as observed for the static bending experiments discussed earlier.

#### **Frequency readout of acoustic vibrations:**

To test the faithfulness of the sensor in reading acoustic vibration, experiments have been carried out by pasting the sensor over a elastic rubber diaphragm. Instead of music, sine wave of known frequency (333, 334, 335 Hz) was feed to the speaker and the resulting acoustic vibrations have been recorded with the sensor. Fourier transform of the current response with time has been done as shown in figure S8d . A sharp spike in the frequency domain matching very close to the input frequency is observed indicating excellent readout of the incident acoustic vibrations by the sensor.

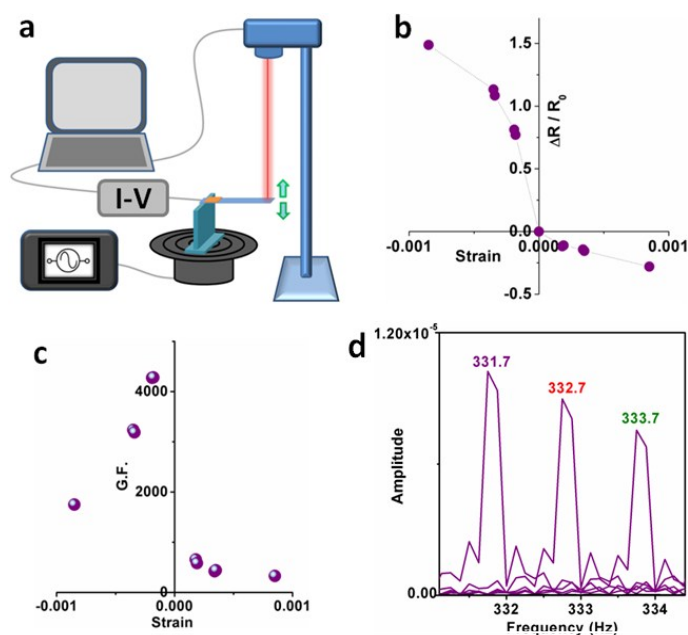


**Figure S8:** (a) Schematic showing the set-up for dynamic straining tests (over vibrating cantilever) of the strain sensor. (b) Relative change in resistance with strain. (c) Gauge factor as a function of strain. (d) The sensor shows excellent frequency readout of acoustic vibrations.

## V. Importance of device geometry in detection of high pressure:

### V.I. Response of partially confined rGO devices to pressure:

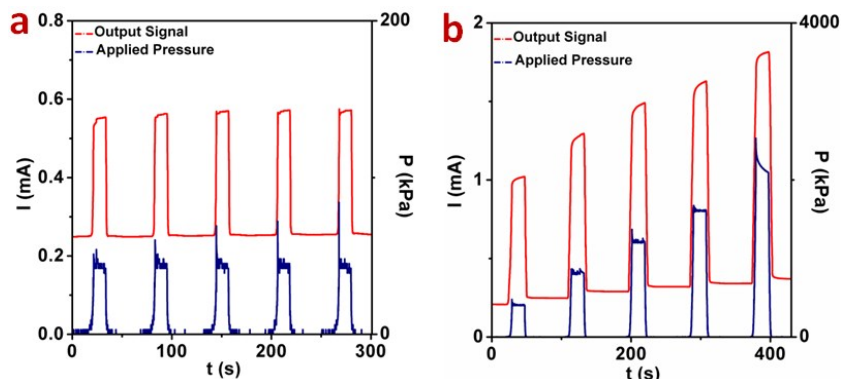


**Figure S9:** (a) Shows repeatability of partially confined rGO devices at low pressure. (b) At higher pressure the base resistance changes significantly after each cycle because of permanent rearrangement of the rGO particles which is due to leaking of the particles from the sides.

### V.II. Response of fully confined rGO devices to pressure:

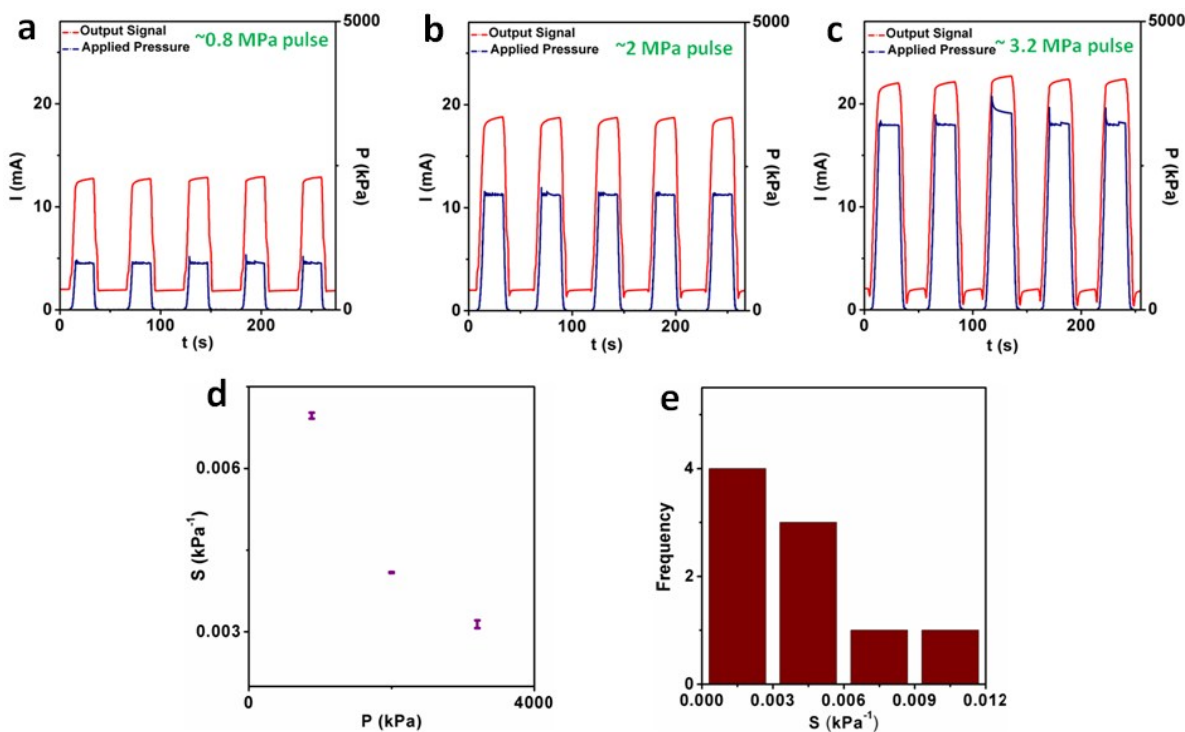


**Figure S10:** (a), (b), (c) Stable response of a fully confined rGO device till high pressure. (d) Sensitivity of the same device at 3 different pressure. (e) Histogram of sensitivity of 10 different devices at a pressure of 880 kPa.

### V.III. Presence of trapped air:

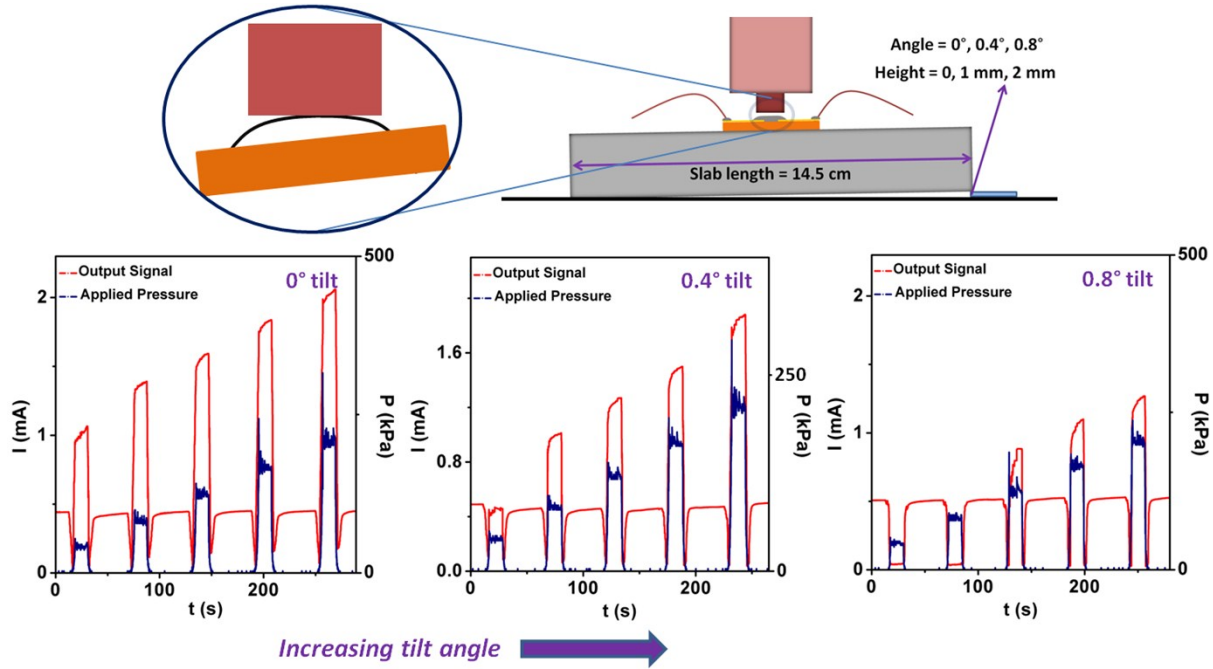


**Figure S11:** Current response of fully confined rGO device to the same set of pulsed pressure with increasing tilt angle of the sensor; 0°, 0.4° and 0.8°. Increasing the tilt angle, increases the threshold pressure (cross-over of current response) indicating that the non-uniform pressing (pressing of one side leads to raising of the other) of the active sensor element (rGO + tape) is responsible for anomalous change in current at low pressure.

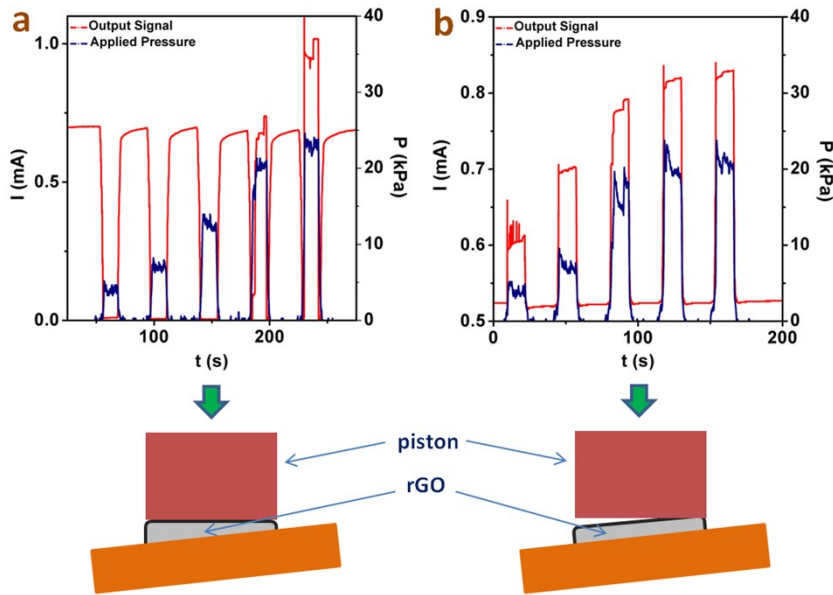


**Figure S12:** (a) Current response at low pressure for fully confined rGO device shows anomaly at low pressure. (b) Current response of the same device with “sides cut” (partially confined rGO device) at the same set of pulsed pressure. The anomaly vanishes indicating that the presence of trapped air in the first case is responsible for raising of the tape at the expense of depression at the other end.

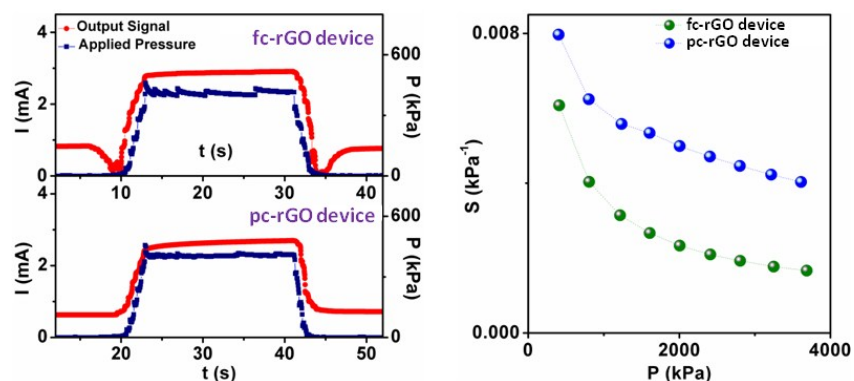


**Figure S13:** (a) Anomaly in response at low pressure for an uncut device (fc-rGO device) which is not present in a cut device (pc-rGO device). (b) Higher sensitivity of cut device than uncut device.

## VI. Effect of elasticity of the tape:

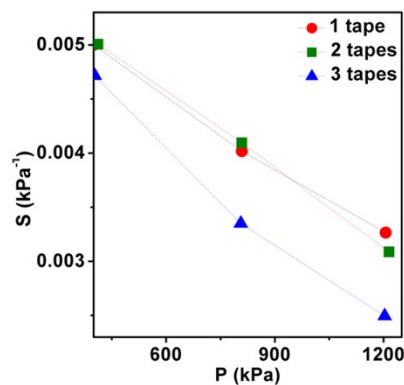


**Figure S14:** Sensivity of the same device with different number of tapes. Increasing the number of tapes onto the same device lead to more initial compression and hence less sensitivity. This also points towards the fact that increasing the layer thickness of rGO keeping the number of tapes same would cause more initial compression and hence lesser sensitivity.

## VII. Low power consumption:

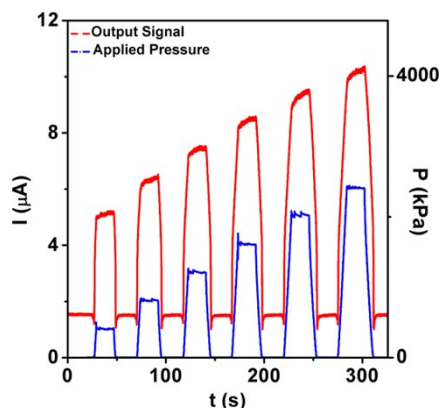


**Figure S15:** Evaluation of performance of the sensor at a lower bias voltage of 1 mV shows a current of few microamperes (base current 1.6  $\mu\text{A}$ ) indicating that the sensor can work at power as low as a few nanowatts (1.6 nW) with good signal to noise ratio.

## VIII. Robustness:

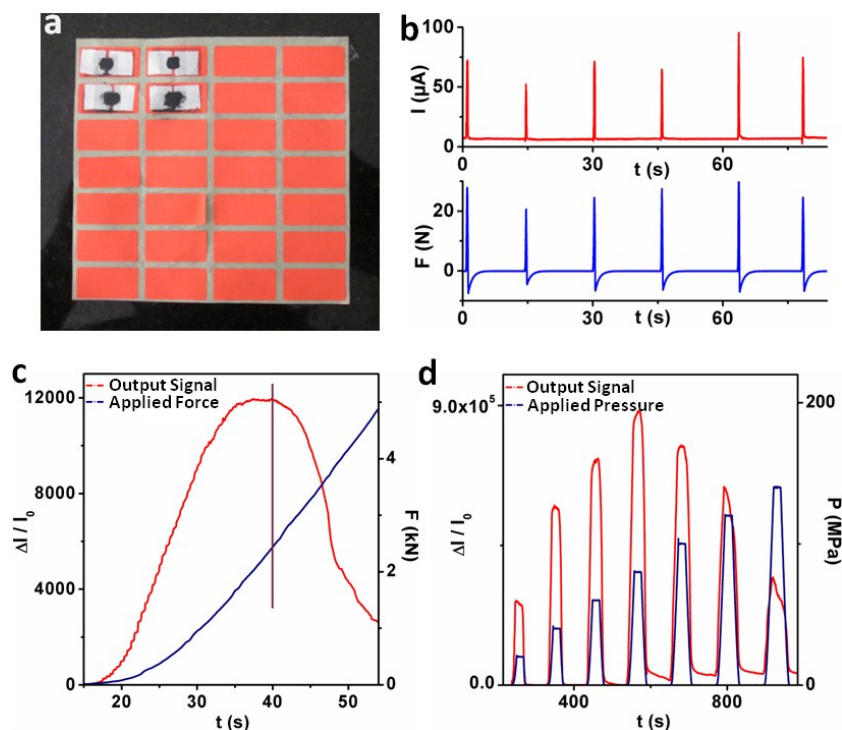


**Figure S16:** (a) Easy device fabrication strategy enables fabrication of device onto adhesive labels. (b) The base current (hence base resistance) of the device remains same even after application of impulsive load over it with the 'Impact Hammer'. (c) Application of force through load cell shows that a typical adhesive label based sensor can withstand forces as large as  $\sim 2.4$  kN ( $\sim 240$  kg). (d) A maximum pressure of 88MPa could be measured with such a adhesive label based device.

## IX. Detection of air pressure:

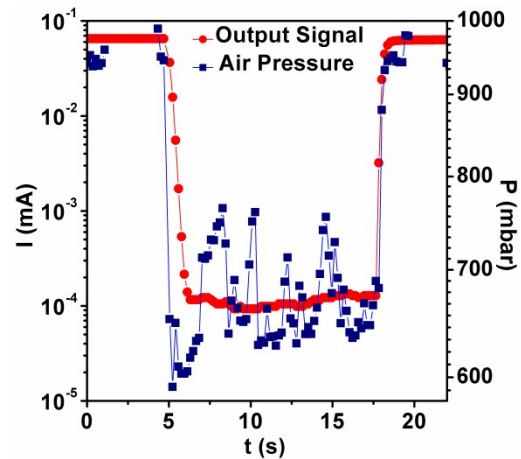


*Figure S17: Detection of fall in air pressure (current shown in red) as the chamber is pumped-out till a pressure of  $\sim 679$  mbar recorded with a reference pirani gauge (pressure shown in blue).*

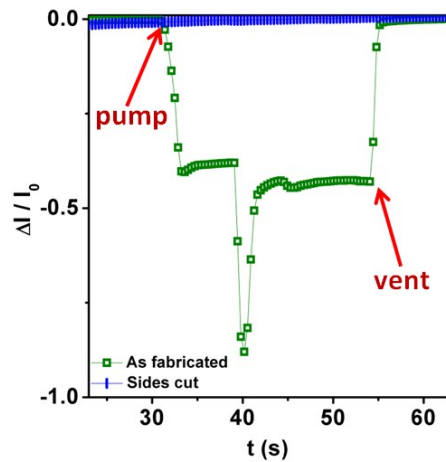


*Figure S18: Current response of the sensor to drop in air pressure (shown in green). The sensor stops responding to air pressure when the tape is punctured (blue flat line) to demolish the air-trapped arrangement.*

## X. Generality of the fabrication strategy:

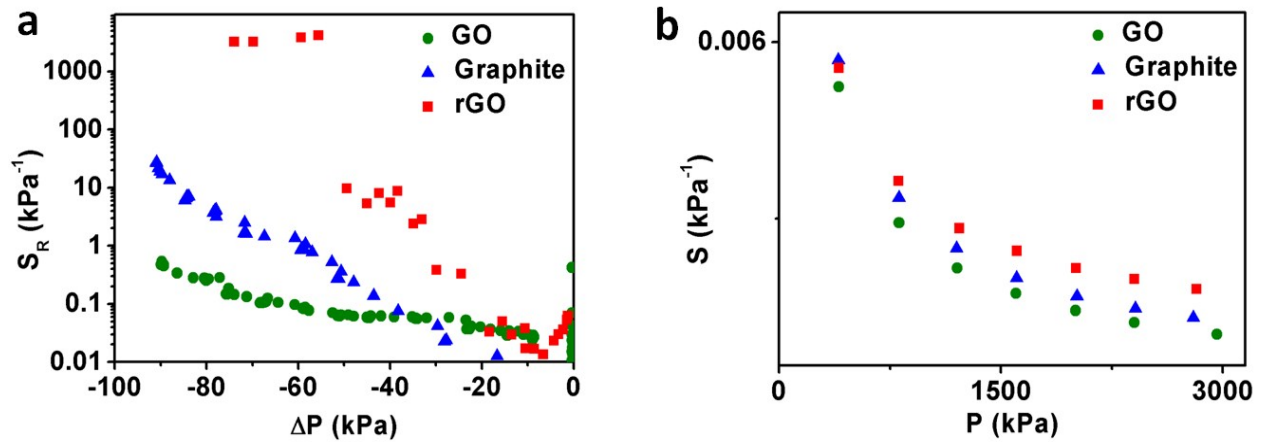


**Figure S19:** The methodology of device fabrication is general and may be applied to other conducting nanomaterials. (a) shows air pressure sensing below atmospheric pressure (expansion of the tape) and (b) compressive pressure (from the piston) sensing. Pressure sensing in compressive and tensile regime of the conducting nanomaterials show that rGO has the best sensitivity in both regimes compared to graphite and GO.

## References:

- 1 Pang, Changhyun et al., A flexible and highly sensitive strain-gauge sensor using reversible interlocking of nanofibres. *Nat. Mater.* 11 (9), 795 (2012).
- 2 Yamada, Takeo et al., A stretchable carbon nanotube strain sensor for human-motion detection. *Nat. Nanotechnol.* 6 (5), 296 (2011).
- 3 Roh, Eun et al., Stretchable, Transparent, Ultrasensitive, and Patchable Strain Sensor for Human-Machine Interfaces Comprising a Nanohybrid of Carbon Nanotubes and Conductive Elastomers. *ACS Nano* 9 (6), 6252 (2015).
- 4 Amjadi, Morteza et al., Highly stretchable and sensitive strain sensor based on silver nanowire-elastomer nanocomposite. *ACS Nano* 8 (5), 5154 (2014).
- 5 Kim, Kyun Kyu et al., Highly Sensitive and Stretchable Multidimensional Strain Sensor with Prestrained Anisotropic Metal Nanowire Percolation Networks. *Nano Lett.* 15 (8), 5240 (2015).
- 6 Hempel, Marek, Nezich, Daniel, Kong, Jing, and Hofmann, Mario, A Novel Class of Strain Gauges Based on Layered Percolative Films of 2D Materials. *Nano Lett.* 12 (11), 5714 (2012).
- 7 Ryu, Seongwoo et al., Extremely Elastic Wearable Carbon Nanotube Fiber Strain Sensor for Monitoring of Human Motion. *ACS Nano* 9 (6), 5929 (2015).
- 8 Li, Xiao et al., Stretchable and highly sensitive graphene-on-polymer strain sensors. *Sci. Rep.* 2, 870 (2012).
- 9 Cohen, Daniel J., Mitra, Debkishore, Peterson, Kevin, and Maharbiz, Michel M., A Highly Elastic, Capacitive Strain Gauge Based on Percolating Nanotube Networks. *Nano Lett.* 12 (4), 1821 (2012).
- 10 Gong, Shu et al., A wearable and highly sensitive pressure sensor with ultrathin gold nanowires. *Nat. Commun.* 5, 3132 (2014).
- 11 Zhou, Jun et al., Flexible Piezotronic Strain Sensor. *Nano Lett.* 8 (9), 3035 (2008).
- 12 Lipomi, Darren J. et al., Skin-like pressure and strain sensors based on transparent elastic films of carbon nanotubes. *Nat. Nanotechnol.* 6 (12), 788 (2011).
- 13 Chelidze, T. and Gueguen, Y., Pressure-induced percolation transitions in composites. *J. Phys. D: Appl. Phys.* 31 (20), 2877 (1998).
- 14 Sahimi, M., Applications of Percolation Theory. *London: Taylor & Francis* (1994).